Improving Satellite-Based Convective Cloud Growth Monitoring with Visible Optical Depth Retrievals

JUSTIN M. SIEGLAFF, LEE M. CRONCE, AND WAYNE F. FELTZ

Cooperative Institute for Meteorological Satellite Studies, University of Wisconsin—Madison, Madison, Wisconsin

(Manuscript received 22 April 2013, in final form 23 September 2013)

ABSTRACT

The use of geostationary satellites for monitoring the development of deep convective clouds has been recently well documented. One such approach, the University of Wisconsin Cloud-Top Cooling Rate (CTC) algorithm, utilizes frequent Geostationary Operational Environmental Satellite (GOES) observations to diagnose the vigor of developing convective clouds through monitoring cooling rates of infrared window brightness temperature imagery. The CTC algorithm was modified to include GOES visible optical depth retrievals for the purpose of identifying growing convective clouds in regions of thin cirrus clouds. An automated objective skill analysis of the two CTC versions (with and without the GOES visible optical depth) versus a variety of Next Generation Weather Radar (NEXRAD) fields was performed using a cloud-object tracking system developed at the University of Wisconsin Cooperative Institute for Meteorological Satellite Studies. The skill analysis was performed in a manner consistent with a recent study employing the same cloud-object tracking system. The analysis indicates that the inclusion of GOES visible optical depth retrievals in the CTC algorithm increases probability of detection and critical success index scores for all NEXRAD fields studied and slightly decreases false alarm ratios for most NEXRAD thresholds. In addition to better identifying vertically growing storms in regions of thin cirrus clouds, the analysis further demonstrates that the strongest cooling rates associated with developing convection are more reliably detected with the inclusion of visible optical depth and that storms that achieve intense reflectivity and large radar-estimated hail exhibit strong cloud-top cooling rates in much higher proportions than they do without the inclusion of visible optical depth.

1. Background

The utility of geostationary satellite data for monitoring growing deep convective clouds has been well documented in the recent literature (Carvalho and Jones 2001; Morel and Senesi 2002; Roberts and Rutledge 2003; Mecikalski and Bedka 2006; Vila et al. 2008; Zinner et al. 2008; Sieglaff et al. 2011; Hartung et al. 2013). These studies have demonstrated the key advantages of geostationary satellites for monitoring deep convective cloud growth, including frequent refresh rate (5–15 min), fine spatial resolution (1–4 km), and expansive coverage (regional to full disk). Additionally, these studies have demonstrated that satellite growth metrics (e.g., cooling infrared brightness temperatures) often provide lead time ahead of other remotely sensed convective development metrics (exceedance of various radar reflectivity thresholds, detection of storm electrification, etc.).

The University of Wisconsin Cloud-Top Cooling Rate (CTC; Sieglaff et al. 2011) algorithm was developed to quantitatively diagnose the vigor of vertical convective cloud growth by determining cooling infrared window brightness temperatures (IRW BTs; see the appendix for a listing of term acronyms and abbreviations used in this paper) between two consecutive Geostationary Operational Environmental Satellite (GOES) imager scans. The CTC output was recently related to future Weather Surveillance Radar-1988 Doppler (WSR-88D) Next Generation Weather Radar (NEXRAD Joint System Program Office 1985) observations in an automated objective manner, testing a hypothesis that developing convective clouds with more intense vertical convective cloud growth (inferred by stronger cloud-top cooling) result in more intense precipitation signatures observed by radar than comparatively weaker vertical convective cloud growth (Hartung et al. 2013, hereinafter

Corresponding author address: Justin Sieglaff, University of Wisconsin—Madison, 1225 West Dayton St., Madison, WI 53706.
E-mail: justins@ssec.wisc.edu

DOI: 10.1175/JAMC-D-13-0139.1

© 2014 American Meteorological Society

H13). This hypothesis was confirmed; more intense CTC signals resulted in higher radar reflectivity, larger vertically integrated liquid (VIL; Greene and Clark 1972), and larger maximum expected size of hail (MESH; Witt et al. 1998a) than clouds with less intense CTC signals. These findings are consistent with previous studies that related cooling rates of IRW BTs to environmental instability and associated updraft/precipitation (Adler and Fenn 1979a,b; Adler et al. 1985; Roberts and Rutledge 2003; Cintineo et al. 2013). Additionally, H13 showed the lead time of CTC signals to the occurrence of the variety of radar field thresholds studied. The lead-time analysis showed the maximum CTC signal of a developing thunderstorm largely occurs *prior* to the development of intense radar signatures. For example, the median lead times of maximum CTC signals to 0.25- and 1.00-in. (1 in. $\simeq$ 2.54 cm) MESHs were 28 and 45 min, respectively. This analysis showed the utility of the CTC algorithm to an operational forecaster, even in regions well covered by radar.

The CTC output is generated in real time at the University of Wisconsin and has been transmitted to the National Oceanic and Atmospheric Administration (NOAA) Hazardous Weather Testbed (HWT), the University of Wisconsin Cooperative Institute for Meteorological Satellite Studies (UW-CIMSS)/National Weather Service (NWS) Milwaukee/Sullivan local HWT, and select NWS Weather Forecast Offices (WFOs) since 2009. The feedback results from NWS forecasters from the 2010 and 2011 testbeds (UW-CIMSS 2013) were largely positive; however, the largest deficiency identified by the 2010–11 testbed participants was the inability to diagnose cooling rates for storms developing in areas of thin cirrus clouds. The CTC algorithm was originally designed to not operate in areas of extensive ice clouds because cooling IRW BTs between two GOES imager scans, in the absence of other information, can be ambiguous. A cooling IRW BT in a scenario with upper-tropospheric cirrus clouds and lower-tropospheric growing cumulus clouds can indicate the following, or a combination of the two: 1) the upper-tropospheric cirrus clouds are growing thicker and hence absorbing more radiation from the lower troposphere and emitting at the colder temperature of the cirrus clouds or 2) the lower cumulus clouds are growing vertically and hence are radiating at corresponding colder temperatures as the cloud grows upward. Using an additional information source from the GOES imager, the retrieved visible optical depth (Walther and Heidinger 2012), can mitigate this ambiguity. In response to the forecaster feedback, the CTC algorithm was improved during early 2012 to address this shortcoming by incorporating the GOES visible optical depth (τ_{vis}) retrievals. The new version of the algorithm was supplied to the NOAA HWT and local NWS WFOs beginning in April 2012 (GOES-R Proving Ground 2013).

The goals of this manuscript are to 1) document the inclusion of τ_{vis} into the CTC algorithm and 2) provide a reader/forecaster a measure of increased CTC algorithm skill by including τ_{vis}. This paper is presented as follows: Section 2 describes the data and methodology used to improve the CTC algorithm. Additionally, some examples are provided to illustrate the improvement of the CTC output by including τ_{vis}. Section 3 provides a statistical analysis of the improved CTC output (CTCv2 or v2) versus CTC output without τ_{vis} (CTCv1 or v1) in a manner consistent with H13. Section 4 summarizes our key findings and provides information for accessing the experimental real-time feed of v2 algorithm output.

2. Data and method

a. Data

GOES-12 imager data over the conterminous United States are used for 23 convectively active afternoons over the central plains during the spring and early summer of 2008 and 2009. The validation domain is consistent with Sieglaff et al. (2011) and H13 (central and southern plains; bounded by 30°–46°N and 94°–104°W) and includes regions of both expected severe thunderstorms and nonsevere thunderstorms. It encompasses convectively active regions with low instability, high instability–high vertical wind shear, and high instability–low vertical wind shear. Possible future work may increase the domain size, allowing for increased sample sizes and for grouping the analysis based upon instability–wind shear combinations. All *GOES-12* data are at the 4-km nadir IR resolution, including visible data (largely for computational efficiency and ease of processing). The *GOES-12* imager data are used in many ways: 1) as input into a cloud-object-tracking system; 2) as input into the GOES cloud mask (Heidinger 2011), cloud phase (Pavolonis 2010), and cloud optical depth retrieval algorithms (Walther and Heidinger 2012); and 3) as input into the CTC algorithm. Quality-controlled NEXRAD 0.01° WSR-88D radar data were provided by the Cooperative Institute for Mesoscale Meteorological Studies at the University of Oklahoma (OU-CIMMS; Lakshmanan et al. 2007). The radar fields used in this study include reflectivity at the −10°C isotherm (Ref_{-10}) (Lakshmanan et al. 2006), VIL, and MESH and are used in the analysis section where CTC output is related to these fields.

b. Method background

The CTC algorithm uses two consecutive GOES imager scans to compute a "box averaged" IRW BT cooling

rate leveraging GOES cloud mask (Heidinger 2011) and GOES cloud phase (Pavolonis 2010) algorithms to identify cloudy satellite pixels and classify the phase (water, supercooled water, mixed, and ice) of the clouds. The CTC methodology utilizes a two-box system: a small box (7×7 satellite pixels) to compute the average IRW BT for cloudy pixels and a large box (13×13 satellite pixels) to compute a variety of metrics. The large-box metrics are used in a series of tests to identify areas of cooling IRW BTs attributed to vertically growing clouds and to eliminate "false" cooling due to horizontal cloud advection. A high-level summary of CTC processing involves the following: 1) computing box-averaged IRW BTs, 2) temporal differencing of box-averaged IRW BTs to produce unfiltered cloud-top cooling rates, and 3) applying a series of tests filtering false cooling rates due to horizontal cloud advection and other undesired artifacts with the end product being the final filtered CTC field. Full details of the CTC algorithm are not included here; the reader is encouraged to reference Sieglaff et al. (2011) for the complete algorithm details. The brief summary given here is intended to provide sufficient background for understanding the description of incorporating τ_{vis} into the CTC algorithm.

The GOES visible optical depth (Walther and Heidinger 2012) is a dimensionless quantity representing the extinction of radiation between the satellite and the earth's surface (Nakajima and King 1990; Platnick et al. 2003). A cloud-free atmosphere will have τ_{vis} near 0 (not absolutely 0 because of trivial gaseous extinction), to small values (up to $\sim$10) for cirrus clouds, and in the tens to $\sim$100 for deep cumuliform clouds (Platnick et al. 2003). As such, significant separation exists between cumuliform clouds and thin cirrus clouds in the retrieved visible optical depth fields. This separation is exploited when incorporating τ_{vis} into v2. Mecikalski et al. (2011) showed the τ_{vis} of immature, yet vertically growing, cumulus clouds reaches a median value of approximately 25, with considerable spread to larger values (larger interquartile value of approximately 75) 0–45 min prior to 35-dBZ rainfall reaching the surface, further motivating the use of optical depth in diagnosing convective development. Figure 1 illustrates τ_{vis} retrievals with more familiar GOES visible and IRW BT imagery (all fields at 4-km GOES resolution) for developing thunderstorms over eastern Illinois–western Indiana valid 1910–1932 UTC 30 March 2012. It is clear from the visible and IRW imagery (Fig. 1) that convective clouds are growing vertically and horizontally and becoming colder. The corresponding τ_{vis} retrievals in this line of developing convection are also increasing with time. It is the collocation of cooling IRW BTs and increasing τ_{vis} retrievals that is exploited to diagnose cloud-top cooling in regions of thin cirrus clouds. The CTC "ice mask" algorithm (Fig. 1, defined below) indicates a large area of thin cirrus clouds that largely prevented v1 from diagnosing the cloud-top cooling rates with these storms (a comparison between v1 and v2 for this case is shown in Fig. 2). The τ_{vis} improvement is used only for solar zenith angles of 70° and less; in regions with solar zenith angles greater than 70°, the v1 logic fully applies with no attempt to include τ_{vis} information.

As mentioned previously, the v1 algorithm was designed to not operate in areas of ice clouds due to the potential ambiguity associated with cooling IRW BTs in these regions. Specifically, the v1 algorithm omits any cooling rates for a pixel in which the large box contains 50% or greater ice cloud fraction (Sieglaff et al. 2011). This ice fraction test omits developing storms beneath thin cirrus clouds and in some cases the strongest cloud-top cooling rates with developing storms when the strongest cooling occurs after the developing storm top had sufficiently glaciated. Note that τ_{vis} has been incorporated into the CTC algorithm and acts as a restoral, meaning the v1 algorithm flow is maintained and the τ_{vis} logic described in this section only acts to add cloud-top cooling rates to the final output field. As such, subsequent skill analysis and comparisons between v2 and v1 are for daytime only (when τ_{vis} retrievals are available). The v2 skill scores are only valid for daytime, while the v1 skill scores as well as the results of H13 apply for nighttime scenes (when τ_{vis} is unavailable).

c. *Incorporating τ_{vis} into the CTC algorithm*

The v1 algorithm utilizes seven tests to remove false cooling rates and these tests are broken into two groups: two major tests that screen out false cooling rates due to horizontal cloud advection and five minor tests to screen out further false cooling rates/undesirable scenarios, such as the ice cloud percentage test mentioned previously. By applying the two major tests to the unfiltered cloud-top cooling rate field to produce an intermediate, partially filtered cloud-top cooling rate field, τ_{vis} is integrated into the CTC algorithm. One additional minor test is applied to this partially filtered cloud-top cooling rate field and screens the cooling rates for clouds determined to be marginally cooling. This minor test can remove vertically growing pixels at the very early stages of growth, but not all cooling clouds within the very early stages of growth will mature into thunderstorms. This test acts to reduce false alarms (Sieglaff et al. 2011). After these three filtering steps are complete, these remaining cloud-top cooling rates are candidates for being restored into the final v2 output field pending the methodology described below.

The τ_{vis} field for both (current and previous) satellite scans is box averaged using the small box previously

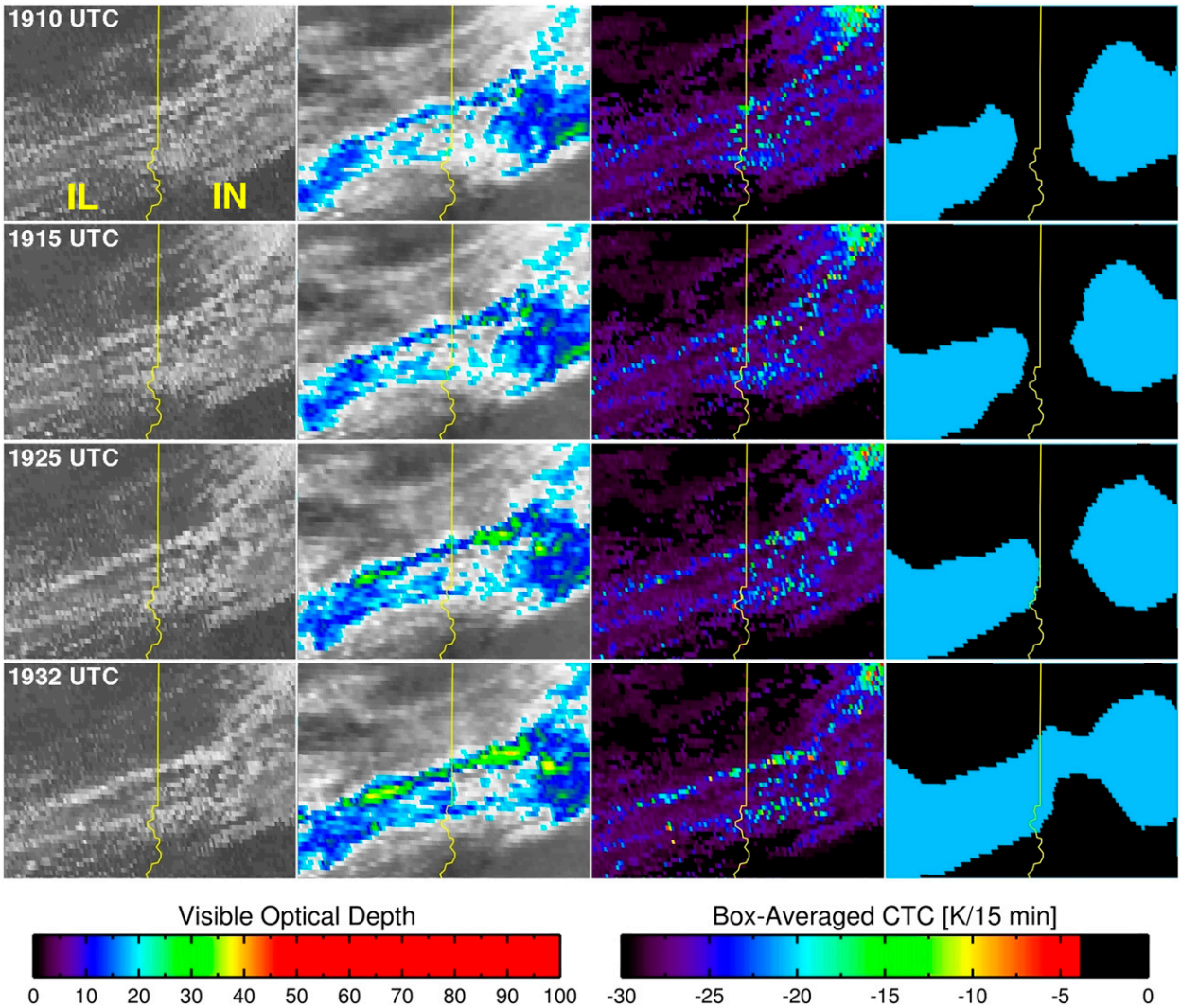

FIG. 1. GOES (left) visible, (center left) 10.7-μm IRW BT, and (center right) visible optical depth retrieval and (right) CTC algorithm ice mask on 30 Mar 2012 over eastern Illinois and western Indiana. A line of developing thunderstorms is evident in the visible and IRW imagery. The increasing visible reflectances and cooling IRW BTs associated with developing thunderstorms are collocated in space and time with increasing retrieved visible optical depth. The ice mask regions are where v1 would not diagnose CTC rates.

described. The partially filtered candidate cloud-top cooling rate pixels are tested for specific conditions related to the τ_{vis} fields. For a pixel to be restored from the partially filtered cloud-top cooling rate field into the final v2 output, the following conditions must be met: 1) the box-averaged τ_{vis} time rate of change must be positive [$>1.0\,(15\,\mathrm{min})^{-1}$] and 2) the maximum box-averaged τ_{vis} within the small box at the current time must be sufficiently large (>25.0). The positive temporal trend of τ_{vis} is straightforward; it should be increasing for vertically growing and horizontally expanding convective cloud. The sufficiently large threshold of 25.0 was chosen based upon Mecikalski et al. (2011). When these conditions within the τ_{vis} fields are met, the partially filtered cloud-top cooling rate is restored into the final v2 output field. Figures 2 and 3 illustrate the improvement of the v2 versus v1 results. The case shown in Fig. 2 is for the same date, time, and location as in Fig. 1; note how v1 only detects cloud-top cooling rates on one developing storm at 1915 and 1925 UTC just east of the Illinois–Indiana border. V2 identifies four additional storms in regions flagged as ice cloud covered (one in eastern Illinois and three additional storms in Indiana; Fig. 2). Figure 3 is another example of improved cloud-top cooling rate detection with v2 for a case of dryline convection in Oklahoma on 14 April 2011. Thin cirrus clouds covered much of Oklahoma at this time (see CTC ice mask; Fig. 3); as such, v1 only detected two storms near the

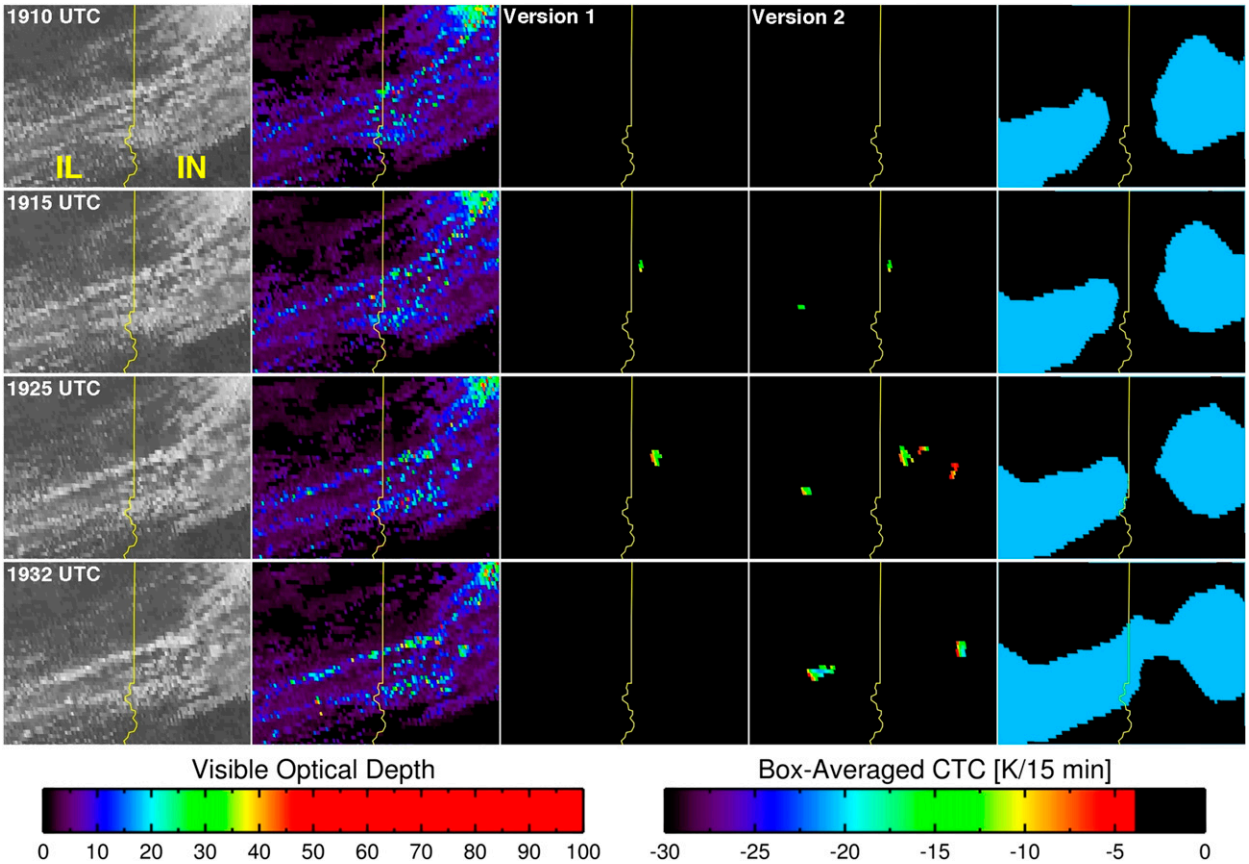

FIG. 2. (left) GOES visible, (center left) GOES visible optical depth retrieval, (center) v1 CTC rates, (center right) v2 CTC rates, and (right) CTC algorithm ice mask on 30 Mar 2012 over eastern Illinois and western Indiana. The v2 algorithm detects more developing thunderstorms than the v1.

Red River at 1940–1955 and 2010 UTC (absence of thin cirrus). The v2 algorithm detected three additional storms over northern Oklahoma between 1955 and 2010 UTC (Fig. 3), as well as the most intense period of cooling of the storm just north of the Red River (2003 UTC), which was missed by v1. These examples demonstrate the improvement of specific cases; the improvement in the form of bulk statistics, over the 23 days studied is presented in the following section.

3. Analysis

a. Background and previous studies

Previous work performed by H13 demonstrated the relationships between v1 output and future NEXRAD observations for developing thunderstorms. H13 used an automated cloud object tracking system that creates cloud objects from GOES imager observations, assigns each object a unique identifier (ID), and tracks these objects through space and time, all while maintaining the unique ID (Sieglaff et al. 2013). The cloud object tracking system utilizes the Warning Decision Support System—Integrated Information (WDSS-II; Lakshmanan et al. 2007) framework developed at the University of Oklahoma to group adjacent cloudy satellite pixels into cloud objects, similar to how a human would analyze satellite or radar data, and track these cloud objects through space and time. A postprocessing utility then merges the WDSS-II output and performs steps to minimize the broken tracks of convective cloud objects. The cloud object tracking system is designed to track convective clouds from infancy *into* their mature phase and provide a means to generate statistics of any number of meteorological fields, as well as temporal trends of such fields for each cloud object within a time period of interest. The object-tracking system supports various geospatial data, including satellite observations, satellite algorithm output (such as CTC output), NEXRAD observations and derived fields, and numerical weather prediction (NWP) data, and so on. The object-tracking system allows for an objective, automated methodology

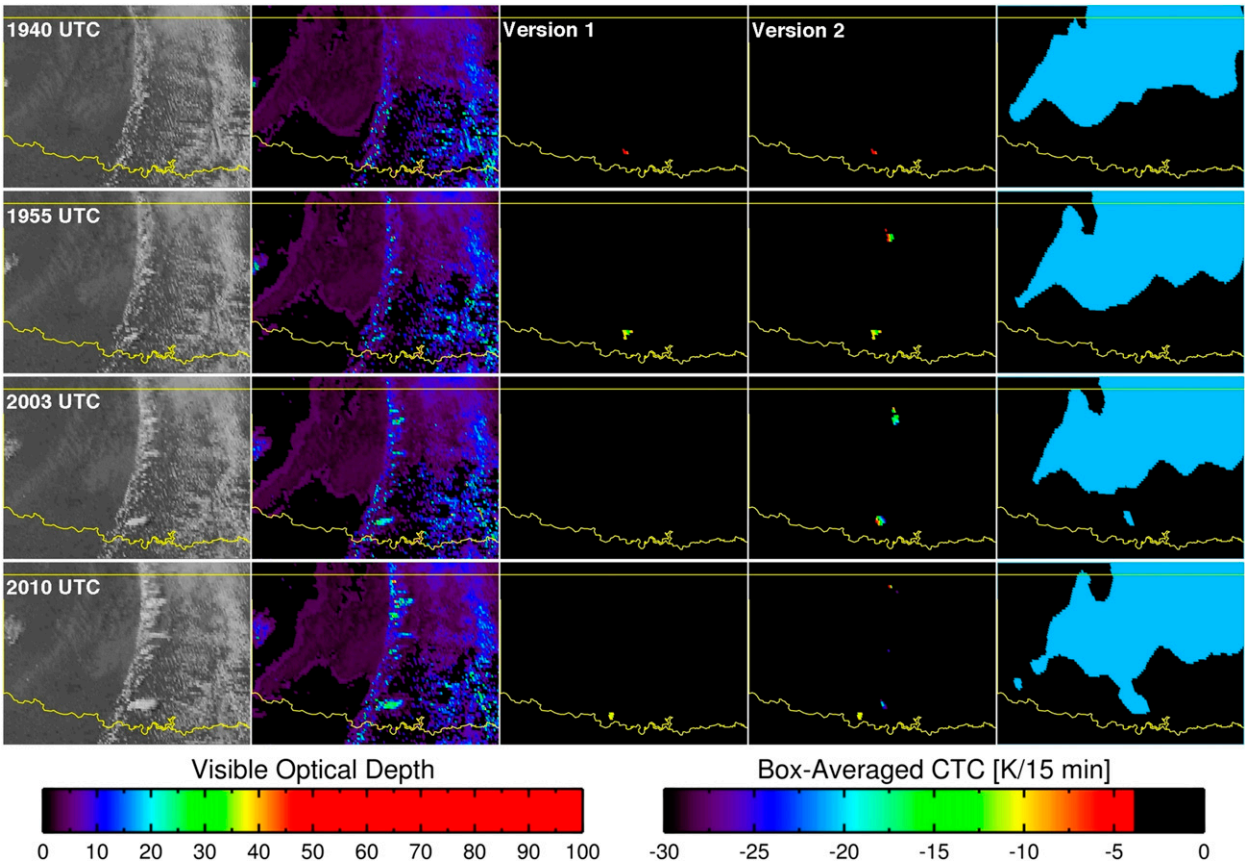

FIG. 3. As in Fig. 2, but for 14 Apr 2011 (top to bottom) over Oklahoma. The v2 algorithm detects more developing thunderstorms than v1 (northern Oklahoma), as well as the most intense period of cooling in the southern storm at 2003 UTC.

to validate and determine relationships between each developing convective cloud's cloud-top cooling rate and future NEXRAD observations, as well as the lead time the CTC signals provide ahead of NEXRAD observations. The details of the convective cloud object tracking system are beyond the scope of this article; full details can be found in Sieglaff et al. (2013).

The analysis presented in this section utilizes the identical framework as that described by H13 and Sieglaff et al. (2013). Consistent with H13, these comparisons do not include comparisons to surface storm reports or severe thunderstorm warnings. While these comparisons would be useful, and are the goals of future work, NEXRAD data and derived output (e.g., MESH) are the focus of this study. Many studies have documented the limitations of storm report data (Witt et al. 1998b; Stumpf et al. 2004; Ortega et al. 2006). Cintineo et al. (2012) demonstrated that multiradar MESH provides superior level of coverage and spatial resolution over storm reports, is free from nonmeteorological biases, and is a good discriminator for the severe-sized hail threshold (1.00 in.). This enables direct comparisons between v1 and v2 for the identical population of cases.

Since v2 is only different from v1 during the daytime (specifically solar zenith angles less than 70°), the comparisons between v1 and v2 are not directly drawn from H13 because that study combined daytime and nighttime scenes. As such, the comparisons between the two CTC versions are for 23 convectively active afternoons (1800–0000 UTC) over the central plains of the United States during the spring and early summer of 2008 and 2009. The total number of cloud objects considered in the verification with valid Ref_{-10} is 3153 and the breakdowns as a function for multiple NEXRAD fields–thresholds are provided in Table 1. The statistical analysis and comparisons presented herein are intended to demonstrate the improved algorithm skill by incorporating τ_{vis} into the CTC algorithm. Similarities and differences of relationships between versions of CTC with NEXRAD observations are also presented.

Consistent with H13, CTC [K $(15\,\mathrm{min})^{-1}$] data points are grouped into three bins (weak, CTC > -10; moderate, $-10 \geq$ CTC > -20; strong, CTC ≤ -20); however, only CTC signals that precede or occur concurrently to the occurrence of a given NEXRAD threshold are counted as hits (e.g., lead times less than 0 min are counted as

TABLE 1. Hit, miss, false alarm, POD, FAR, and CSI statistics for CTC [v1 and v2 (boldface)] and radar reflectivity threshold at the −10°C isotherm (Ref_{-10}) for the interior plains region of the United States for the 23 convective days within the validation dataset. Hit and miss counts include all hits and misses for $Ref_{-10} \geq$ the bin value. False alarm counts include cloud objects that had a CTC signal and no Ref_{-10} value, as well as those objects that had a cooling rate and achieved a maximum $Ref_{-10} <$ the bin value. A hit is defined as any cloud object that was assigned a CTC rate and also achieved a Ref_{-10} value of the corresponding bin magnitude or greater during its lifetime. A miss is a cloud object that achieved a Ref_{-10} magnitude that was ≥ the bin value during its lifetime but was never assigned a CTC rate, or any cloud object that achieved a $Ref_{-10} \geq$ the corresponding bin *prior to* it being assigned a corresponding CTC rate. The italicized POD, FAR, and CSI values are for all CTC values without distinction for CTC magnitude.

	Weak ($Ref_{-10} <$ 35 dBZ)		Moderate ($35 \leq Ref_{-10} < 60$ dBZ)										Strong ($Ref_{-10} \geq$ 60 dBZ)	
Reflectivity at −10°C	<35 dBZ		35 dBZ		40 dBZ		45 dBZ		50 dBZ		55 dBZ		≥60 dBZ	
Total No. of hits	**302**	260	**225**	194	**190**	169	**160**	138	**128**	108	**93**	78	**55**	45
Total No. of misses	**2851**	2893	**897**	928	**563**	584	**326**	348	**160**	180	**69**	84	**22**	32
Total No. of false alarms	**215**	174	**231**	190	**232**	189	**233**	191	**224**	188	**224**	190	**238**	208
POD														
All CTC	***0.10***	*0.08*	***0.20***	*0.17*	***0.25***	*0.22*	***0.33***	*0.28*	***0.44***	*0.38*	***0.57***	*0.48*	***0.71***	*0.58*
CTC > −10	**0.02**	0.03	**0.03**	0.05	**0.03**	0.06	**0.04**	0.07	**0.04**	0.09	**0.04**	0.09	**0.03**	0.08
−10 ≥ CTC > −20	**0.04**	0.04	**0.08**	0.08	**0.10**	0.10	**0.12**	0.12	**0.15**	0.16	**0.13**	0.18	**0.14**	0.21
CTC ≤ −20	**0.03**	0.02	**0.09**	0.05	**0.12**	0.07	**0.17**	0.09	**0.25**	0.13	**0.41**	0.21	**0.55**	0.30
FAR														
All CTC	***0.42***	*0.40*	***0.51***	*0.49*	***0.55***	*0.53*	***0.59***	*0.58*	***0.64***	*0.64*	***0.71***	*0.71*	***0.81***	*0.82*
CTC > −10	**0.08**	0.14	**0.11**	0.19	**0.13**	0.21	**0.15**	0.24	**0.16**	0.25	**0.18**	0.28	**0.18**	0.30
−10 ≥ CTC > −20	**0.19**	0.16	**0.23**	0.20	**0.25**	0.22	**0.27**	0.23	**0.28**	0.26	**0.31**	0.29	**0.34**	0.34
CTC ≤ −20	**0.14**	0.09	**0.16**	0.11	**0.17**	0.10	**0.18**	0.11	**0.20**	0.13	**0.22**	0.14	**0.29**	0.17
CSI														
All CTC	***0.09***	*0.08*	***0.17***	*0.15*	***0.19***	*0.18*	***0.22***	*0.20*	***0.25***	*0.23*	***0.24***	*0.22*	***0.17***	*0.16*
CTC > −10	**0.02**	0.03	**0.04**	0.05	**0.04**	0.06	**0.05**	0.08	**0.05**	0.09	**0.05**	0.09	**0.03**	0.05
−10 ≥ CTC > −20	**0.04**	0.04	**0.08**	0.08	**0.10**	0.10	**0.12**	0.12	**0.14**	0.15	**0.11**	0.15	**0.08**	0.12
CTC ≤ −20	**0.04**	0.02	**0.09**	0.05	**0.13**	0.07	**0.18**	0.11	**0.24**	0.15	**0.32**	0.22	**0.28**	0.23

misses), while H13 counted CTC signals with lead time of −17 min and greater as hits; therefore, comparisons between this study and H13 need to account for this difference.

b. Caveats applicable to statistical analysis

The subsequent section presents a skill analysis for the two versions of CTC versus three NEXRAD fields; however, a discussion related to the limitations of the automated objective validation technique and how to interpret the resultant statistics is first necessary. The automated cloud object tracking system (used by H13 and herein) was designed to track growing convective clouds from infancy *into* satellite maturity (presence of thunderstorm anvils). Ultimately, thunderstorm anvils merge together and the tracking of separate thunderstorms becomes difficult, if not impossible, only using satellite data. While efforts were made to track storms as long as possible, tracking of any specific storm could end prior to achieving maximum intensity as defined by a variety of NEXRAD metrics (H13; Sieglaff et al. 2013). This has a direct impact on the statistical analysis of probability of detection (POD), false alarm ratio (FAR), and critical success index (CSI). Specifically, there is an underrepresentation of extreme NEXRAD values (intense reflectivity, large estimated hail size, etc.) within the validation framework. *As such, for increasing NEXRAD intensity, the POD values are likely underestimates and the FAR values are likely overestimates* (H13)*, thereby leading the CSI scores to be underestimates*. Consider the following example: A developing storm with valid CTC signal is tracked successfully to a point of reaching 55-dBZ reflectivity, 0.25-in. MESH, and 30 kg m^{-2} VIL; thereafter, the storm is no longer tracked since it merged into a large anvil mass. For NEXRAD fields greater than these values, that cloud-top cooling rate is counted as a false alarm. Additionally, the number of hits at extreme values is also decreased, and since such a storm had a valid cloud-top cooling rate, the POD and CSI scores are likewise decreased. As a final point, the validation domain is expansive and not limited to only regions of expected severe weather, so a proportion of the storms in the analysis should not be expected to reach intense/severe NEXRAD values. As such, the expanse of the validation domain acts to decrease POD/CSI for these intense/severe NEXRAD values more so than if one only considers regions supportive for severe thunderstorms. While these caveats

TABLE 2. Counts of cloud objects in the validation scheme with maximum observed CTC and any measured value of the radar-derived fields broken down by CTC intensity for v1 (first three rows) and v2 (last three rows) in the validation domain.

Max CTC rate intensity [K (15 min)$^{-1}$]	Ref_{-10}	VIL	MESH
v1 > −10	83	32	18
−10 ≥ v1 > −20	114	72	41
v1 ≤ −20	63	48	37
v2 > −10	58	17	5
−10 ≥ v2 > −20	135	85	32
v2 ≤ −20	109	102	82

TABLE 3. Counts of cloud objects for all CTC and any measured value of the radar-derived fields broken down by CTC intensity for v1 (first three rows) and v2 (last three rows) in the validation domain. All CTC refers to all cooling rates exhibited by a single cloud object. For example, if a cloud object exhibited weak, moderate, and strong CTC at different times of growth, the cloud object would be counted in each CTC bin, as opposed to only the strong CTC bin in Table 2. As such, Table 3 has more counts than Table 2.

All CTC rate intensity [K (15 min)$^{-1}$]	Ref_{-10}	VIL	MESH
v1 > −10	151	91	47
−10 ≥ v1 > −20	172	125	77
v1 ≤ −20	79	64	50
v2 > −10	159	107	59
−10 ≥ v2 > −20	259	191	115
v2 ≤ −20	164	156	128

are imperative to consider when assessing the specific performance scores, the statistical differences between the two CTC algorithms are impacted identically, so relative changes can be attributed solely to algorithm modifications and not to any validation framework shortcomings.

c. *NEXRAD-derived skill analysis*

1) REFLECTIVITY AT −10°C

Table 1 shows hits, misses, false alarms, PODs, FARs, and CSIs for v2 (boldface) and v1 for Ref_{-10}. Table 2 shows the *total number of cloud objects* having a valid NEXRAD signal and valid cloud-top cooling rate broken down by cooling rate strength, and these totals are only for the *maximum* cloud-top cooling rate observed in a cloud object's lifetime (valid means there were nonmissing NEXRAD and CTC values for a given cloud object). As such, these totals equal the hits in Table 1 for the two CTC versions. Table 3 shows the *total instances* of cloud objects having a valid NEXRAD signal and valid CTC signal for each CTC strength bin (a single cloud object could potentially be counted in each CTC bin). For example, a storm may initially have a weak CTC signal, the following scan have a moderate CTC signal, and then later exhibit a strong CTC signal; therefore, Table 3 has a larger population than Table 2.

The v2 exhibits an increase in hits (and decrease in misses) for all Ref_{-10} bins (Table 1). The POD for strong to intense Ref_{-10} (50 dBZ and larger) increases for v2 versus v1 with a general rise of 0.06–0.13 (from 0.38–0.58 to 0.44–0.71). Further examination of POD metrics indicates the majority of storms achieving strong to intense Ref_{-10} exhibited strong cloud-top cooling rates in v2 and at a much higher proportion than that of v1. The increased proportion of strong CTC values for v2 is due to increased data points added by the τ_{vis} algorithm methodology. In v1, the ice cloud percentage test often prevented the strongest cooling rate from being diagnosed; in some cases only the initial cooling rate was diagnosed (belonging to weak or moderate bins). The inclusion of the τ_{vis} trend and magnitude into the v2 algorithm allows for more successful identification of the strongest cooling rate (note the much larger fraction of strong cooling rates for v2 than v1 in Table 2, in addition to more storms being diagnosed). Despite a small increase in the total number of false alarms in v2 than v1, the FAR increases only slightly for Ref_{-10} 45 dBZ and less and remains unchanged or slightly decreases for Ref_{-10} 50 dBZ and larger (Table 1).

The increased POD and decreased FAR for Ref_{-10} translate into slightly increased CSI scores for v2 over v1 (Table 1) when assessing total CSI, but when considering only the strong CTC hits, the CSI scores increase by larger proportions, especially for strong–intense Ref_{-10}. The largest CSI value for all CTC occurs at 50 dBZ (0.27 for v2; 0.23 for v1) and at 55 dBZ when considering only the strong CTC (0.32 for v2; 0.22 for v1). The implication of maximum CTC skill for storms achieving 50 or 55 dBZ at Ref_{-10} should be taken with caution, however. Recall the previous discussion related to cloud object tracking limitations. While not every storm that achieves 50 dBZ will go on to reach 55 or 60 dBZ, the cloud object tracking limitations compound the decrease in the number of storms reaching more intense values. Attempts to definitively declare the CTC algorithm to be most skillful for a specific reflectivity threshold should be made with caution, but the relative increase in skill between v2 and v1 is unaffected by these concerns.

In general, v2 exhibits more skill in identifying storms for all values of Ref_{-10} than v1 with the most notable increase for moderate–strong Ref_{-10}. The v2 (relative to v1) algorithm identifies more storms with a POD as high as 0.71 (0.58) for 60-dBZ Ref_{-10}. Additionally, the

TABLE 4. As in Table 1, but with radar-estimated MESH.

MESH (in.)	0.25		0.50		0.75		1.00		1.50		≥2.00	
Total No. of hits	**119**	96	**103**	80	**77**	62	**62**	50	**40**	32	**25**	20
Total No. of misses*	**68**	91	**51**	80	**23**	38	**13**	25	**4**	12	**2**	7
Total No. of false alarms	**203**	178	**211**	184	**222**	196	**227**	200	**246**	215	**262**	227
POD												
All CTC	***0.64***	*0.51*	***0.67***	*0.52*	***0.77***	*0.62*	***0.83***	*0.67*	***0.91***	*0.73*	***0.93***	*0.74*
CTC > −10	**0.03**	0.09	**0.03**	0.09	**0.02**	0.11	**0.01**	0.09	**0.00**	0.09	**0.00**	0.07
−10 ≥ CTC > −20	**0.17**	0.21	**0.16**	0.21	**0.12**	0.23	**0.15**	0.24	**0.14**	0.27	**0.19**	0.30
CTC ≤ −20	**0.44**	0.21	**0.48**	0.21	**0.63**	0.28	**0.67**	0.33	**0.77**	0.36	**0.74**	0.37
FAR												
All CTC	***0.63***	*0.65*	***0.67***	*0.70*	***0.74***	*0.76*	***0.79***	*0.80*	***0.86***	*0.87*	***0.91***	*0.92*
CTC > −10	**0.17**	0.27	**0.17**	0.27	**0.18**	0.28	**0.19**	0.30	**0.19**	0.31	**0.19**	0.32
−10 ≥ CTC > −20	**0.29**	0.26	**0.30**	0.29	**0.33**	0.32	**0.34**	0.34	**0.35**	0.36	**0.36**	0.38
CTC ≤ −20	**0.17**	0.12	**0.20**	0.14	**0.23**	0.16	**0.26**	0.16	**0.32**	0.20	**0.37**	0.22
CSI												
All CTC	***0.31***	*0.26*	***0.28***	*0.24*	***0.24***	*0.21*	***0.21***	*0.18*	***0.14***	*0.12*	***0.09***	*0.08*
CTC > −10	**0.04**	0.10	**0.05**	0.09	**0.03**	0.09	**0.01**	0.07	**0.00**	0.04	**0.00**	0.02
−10 ≥ CTC > −20	**0.17**	0.20	**0.14**	0.18	**0.09**	0.16	**0.09**	0.14	**0.05**	0.11	**0.05**	0.07
CTC ≤ −20	**0.40**	0.23	**0.40**	0.23	**0.41**	0.26	**0.36**	0.28	**0.26**	0.21	**0.16**	0.14

increased identification of the strongest cooling rates (and associated large percentage of strong Ref_{-10} values) by v2 can lend to increased confidence that a developing storm should exhibit a strong CTC signal if strong Ref_{-10} is to be achieved later in the storm's life cycle than one would expect with v1.

2) MAXIMUM EXPECTED SIZE OF HAIL

Table 4 shows hits, misses, false alarms, PODs, FARs, and CSIs for v2 (boldface) and v1 for MESH. Similar to Ref_{-10}, the number of hits increased (and misses decreased) for all values of MESH. The POD significantly improves by 0.15–0.20 for all total MESH bins. V2 captures 64% of all storms generating any hail (0.25+-in. MESH) and 83% of storms with radar-estimated severe hail (1.00+ in.) while v1 only achieved 51% and 67% for these MESH thresholds. The majority of all storms producing any hail (0.25+-in. MESH) exhibit strong v2s. Effectively every storm exhibiting radar-estimated severe hail (1.00+-in. MESH) had moderate or strong cloud-top cooling rates in v2; much less of a definite relationship is observed with v1. The proportion of storms reaching the strong CTC bin is again much higher for v2 than v1 as a result of τ_{vis} enabling detection of each storm's strongest cooling rate (Tables 2 and 4). The FAR values are generally slightly smaller for v2 than v1 when considering all CTC data points. This translates into increased CSI scores for v2 relative to v1. The CSI scores for the total CTC bins generally increase slightly for v2 relative to v1, but when only considering the strongest CTC bin, the skill increases by as much as ~0.15.

Like with Ref_{-10}, the apparent decrease in skill for increasing MESH needs to be taken in context. The validation domain contains storms within regions where severe convection was not expected and the limitations of the cloud object tracking system contribute to fewer storms reaching severe hail sizes than actually occur. Perhaps the most useful skill metric is the v2 POD numbers (0.83 for 1.00+-in. MESH, 0.91 for 1.50+-in. MESH). These extremely high POD numbers suggest that when the environment is supportive for severe hail, a forecaster can have very high confidence the v2 algorithm will identify a storm that will achieve radar-estimated severe hail and likely have a strong CTC (Table 4). While the FAR values are quite high, this is expected because severe hail is quite rare relative to all thunderstorms (consider count decreases from Ref_{-10} to MESH in Table 2 and the prior statement that valid cloud-top cooling rates with no associated NEXRAD bin values are counted as false alarms). Also, the FAR values, while high, are slightly lower than the POD numbers for v2.

Overall, v2 is shown to be more skillful in diagnosing storms that produce any radar-estimated hail (0.25+-in. MESH), with high PODs for storms producing severe MESHs. Of most significance is that the very large proportion of storms that produce radar-estimated hail exhibit strong CTC. Again, this suggests to a forecaster that in an environment supportive of hail development, any developing storm that will produce hail, particularly severe hail, should be expected to exhibit strong CTC, especially with v2.

3) VERTICALLY INTEGRATED LIQUID (VIL)

Table 5 shows hits, misses, false alarms, PODs, FARs, and CSIs for v2 (boldface) and v1 for VIL. The various

TABLE 5. As in Table 1, but with radar VIL.

VIL ($kg\,m^{-2}$)	5		10		20		30		40		≥50	
Total No. of hits	**204**	158	**169**	128	**121**	96	**84**	66	**63**	48	**40**	35
Total No. of misses*	**287**	333	**191**	232	**87**	112	**32**	50	**23**	28	**5**	10
Total No. of false alarms	**202**	183	**202**	183	**213**	186	**216**	192	**226**	202	**246**	212
POD												
All CTC	***0.42***	*0.32*	***0.47***	*0.36*	***0.58***	*0.46*	***0.72***	*0.57*	***0.83***	*0.63*	***0.89***	*0.78*
CTC > −10	**0.03**	0.08	**0.04**	0.09	**0.03**	0.10	**0.03**	0.10	**0.01**	0.09	**0.00**	0.07
−10 ≥ CTC > −20	**0.17**	0.15	**0.17**	0.15	**0.17**	0.18	**0.14**	0.22	**0.13**	0.22	**0.11**	0.31
CTC ≤ −20	**0.21**	0.10	**0.26**	0.11	**0.38**	0.18	**0.56**	0.25	**0.68**	0.32	**0.78**	0.40
FAR												
All CTC	***0.50***	*0.54*	***0.54***	*0.59*	***0.64***	*0.66*	***0.72***	*0.74*	***0.78***	*0.81*	***0.86***	*0.86*
CTC > −10	**0.15**	0.23	**0.16**	0.24	**0.17**	0.27	**0.18**	0.28	**0.19**	0.30	**0.19**	0.31
−10 ≥ CTC > −20	**0.21**	0.21	**0.24**	0.23	**0.28**	0.26	**0.32**	0.31	**0.34**	0.34	**0.36**	0.36
CTC ≤ −20	**0.14**	0.10	**0.15**	0.12	**0.19**	0.13	**0.22**	0.15	**0.25**	0.16	**0.31**	0.19
CSI												
All CTC	***0.29***	*0.23*	***0.30***	*0.24*	***0.29***	*0.24*	***0.25***	*0.21*	***0.21***	*0.17*	***0.14***	*0.14*
CTC > −10	**0.05**	0.08	**0.05**	0.09	**0.04**	0.10	**0.03**	0.09	**0.01**	0.06	**0.00**	0.03
−10 ≥ CTC > −20	**0.19**	0.15	**0.18**	0.15	**0.16**	0.17	**0.11**	0.16	**0.08**	0.13	**0.04**	0.13
CTC ≤ −20	**0.23**	0.12	**0.28**	0.13	**0.35**	0.20	**0.40**	0.25	**0.38**	0.26	**0.27**	0.24

skill metrics for VIL exhibit very similar improvements as for Ref_{-10} and MESH. For brevity an in-depth analysis of VIL is omitted, but Table 5 shows the full statistics. The most important points are that, in general, the POD numbers are again improved for all VIL thresholds for v2 relative to v1 with very high POD (>0.80) for VIL of $40\,kg\,m^{-2}$ and larger. The largest CSI scores are associated with strong CTC values, suggesting a forecaster should expect strong CTC values (especially for v2) with any developing storm in regions where large VIL totals are anticipated.

d. CTC and maximum NEXRAD distributions

Using the hits from Tables 1, 4, and 5, distributions of the maximum radar value achieved (for Ref_{-10}, MESH, and VIL) versus all CTC and maximum CTC were constructed. Figures 4–6 show distributions of all and maximum CTC versus maximum NEXRAD values achieved for Ref_{-10}, MESH, and VIL, respectively. In Figs. 4–6, the left panels are for v2 and the right panels are for v1; the top panels correspond to all CTC (any storm may have more than one valid cloud-top cooling rate diagnosed) and the bottom panels correspond to a cloud object's maximum cloud-top cooling rate observed.

The distributions in Figs. 4a and 4c show generally wide distributions for all CTC versus maximum Ref_{-10} for each CTC bin. The weak and moderate CTC bins do not show any appreciable differences between the two algorithm versions; however, the strong bin for v2 (Fig. 4a) has a significantly more narrow distribution (bottom 1σ value is 40 dBZ instead of 30 dBZ and the 25th-percentile value is 45 dBZ instead of 40 dBZ) and has a larger median Ref_{-10} of 55 dBZ instead of 50 dBZ. The narrower distribution width and larger median suggest the added strong CTC points of v2 are more often associated with storms that achieve more intense Ref_{-10}, which agrees with the skill score analysis. Figures 4b and 4d are the same as Figs. 4a and 4c except only the maximum CTC for a cloud object is considered. The distributions in Figs. 4b and 4d are significantly narrower when compared with all CTC results (Figs. 4a,c), simply because the initial weaker growth of strong storms is omitted in the maximum CTC distributions (included in all of the CTC distributions). The v2 distributions (Fig. 4b) are generally narrower [toward larger (smaller) Ref_{-10} for the strong (weak) CTC bin] than those for v1 (Fig. 4d). The narrowing and shift toward smaller Ref_{-10} for the weak CTC is attributed to the increased diagnosis of strong cooling rates with v2. The better diagnosis of strong cooling rates, in turn, results in the weak CTC bin to be populated with storms that never actually achieve moderate or strong cooling rates as opposed to storms that did have strong growth but the strong growth period was missed in v1. This narrowing and the shift toward larger Ref_{-10} for the strong CTC occurs for similar reasons; the added data points are largely from storms that achieve strong to intense Ref_{-10} (Table 2: 109 strong for v2; 63 strong for v1). These distributions give increased confidence that a strong cooling rate from v2 will result in strong to intense Ref_{-10} and that a developing storm with only weak cooling in v2 will, in general, not develop strong to intense Ref_{-10} when compared to v1.

Figure 5 is the same as Fig. 4 but is for MESH. Similar relationships exist between all CTC and maximum MESH results (Figs. 5a,c), as shown with Ref_{-10}. The v2 distributions for weak and moderate are more

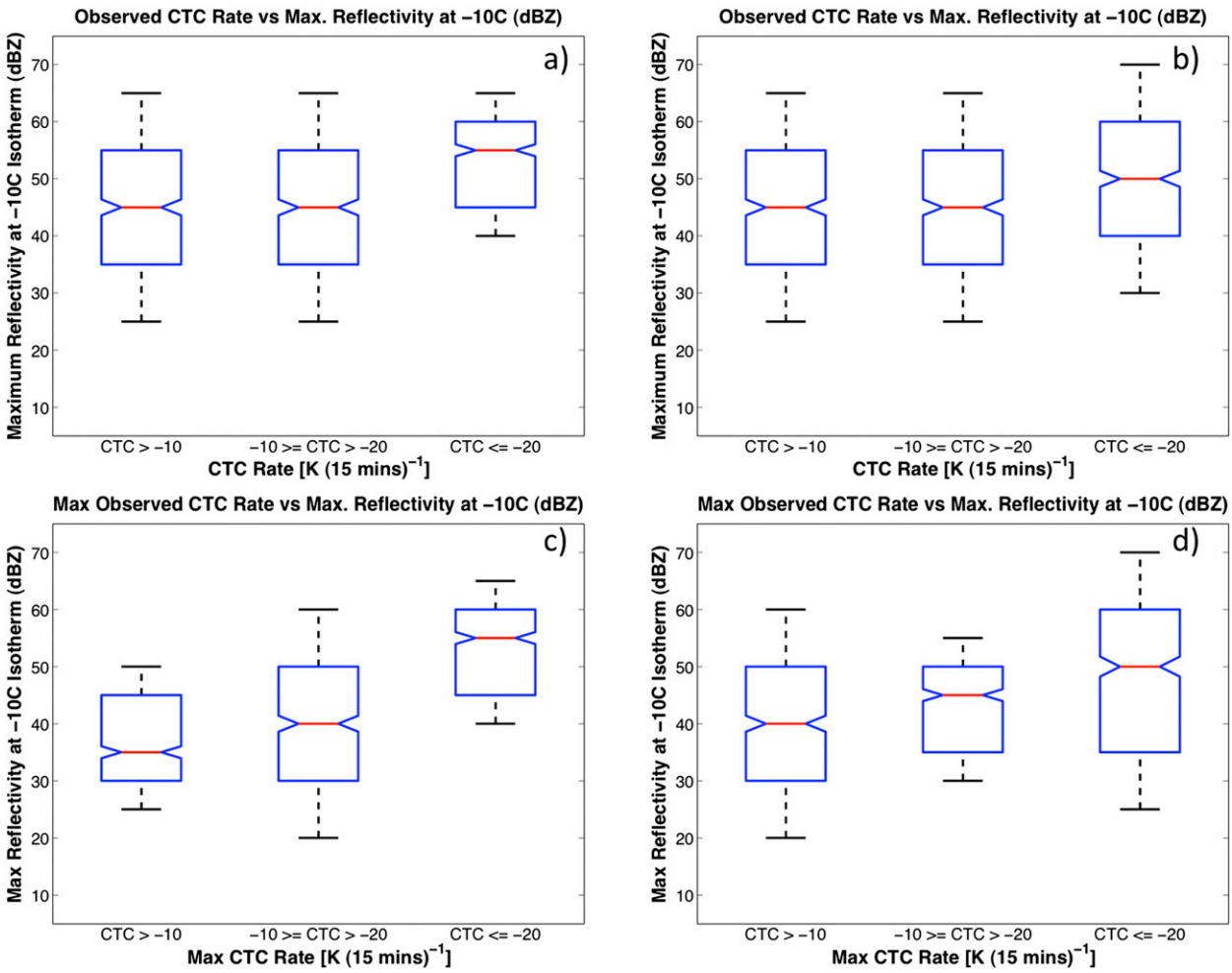

FIG. 4. Comparison of (a),(b) all instantaneous and (c),(d) maximum CTC values with maximum reflectivity at −10°C isotherm [Ref_{-10}; dBZ] for (left) v2 and (right) v1 for cloud objects that had both a CTC and associated Ref_{-10} at some point in their lifetime. CTC rates for cloud objects are binned by intensity [K (15 min)$^{-1}$] with weak, moderate, and strong convective growth rates defined as CTC > -10, $-10 \geq$ CTC > -20, and CTC ≤ -20, respectively. For each boxplot, the median (red line), 25th and 75th percentiles (lower and upper bounds of the blue box), and one standard deviation (whiskers) are shown. The medians of different intensity bins are significantly different at the 5% significance level if the widths of the notches centered on the medians do not overlap.

constrained to smaller MESH values than for v1, while the strong CTC bin is largely the same. When considering the maximum CTC (Figs. 5b,d), the distributions are again much narrower for v2 than v1 for similar reasons to those with Ref_{-10}. [The weak bin in Fig. 5b is very narrow largely because of a very small sample size (six storms had a maximum v2 in the weak bin and 0.25+-in. MESH).] When considering maximum CTC, v2 (Fig. 5b) has much narrower distributions shifted to smaller MESH values in the weak and moderate bins than does v1 (Fig. 5d), as well as smaller populations (Table 2). The strong bin is largely the same between the two CTC versions. Figures 5b and 5d imply that one can more confidently expect radar-estimated severe hail (1.00+ in.) when a developing storm exhibits strong cloud-top cooling rates in v2 than was possible with v1 (where severe hail was more common in the weak and moderate CTC bins).

Figure 6 is the same as Figs. 4 and 5 but is for VIL. Again, for brevity, a full analysis of Fig. 6 is omitted. The key points taken from Fig. 6 are similar to those of Figs. 4 and 5; a forecaster can have increased confidence that a developing storm with strong (weak) v2 will more likely produce large (small) VIL values in the future than could be deduced from the analysis of v1.

H13 included a lead-time analysis of the CTC signal (both all and maximum) ahead of maximum NEXRAD values obtained for each storm, as well as lead time ahead of operationally significant thresholds (e.g., MESH of 1.00 in. and VIL of 40 kg m^{-2}). The lead time from H13 indicates a 20- (60+-) minute lead time for VIL values of

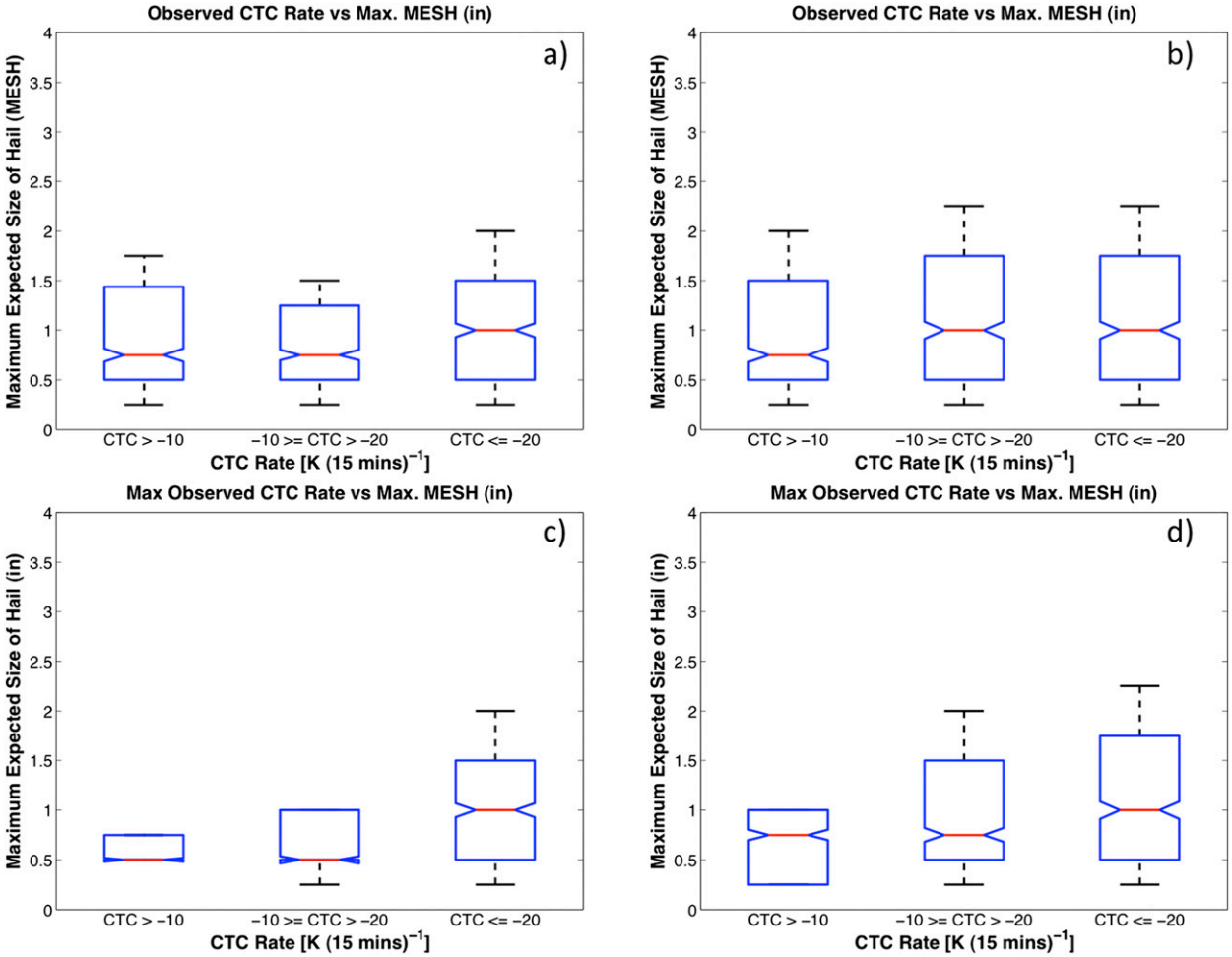

FIG. 5. As in Fig. 4, but for comparison with MESH (in.).

20 (45) kg m^{-2} and a 45-min lead time for severe hail MESH (1.00 in.). While the lead-time threshold that defines hits differs between H13 and this manuscript (−17 and 0 min, respectively), the lead times determined herein were very similar to those reported by H13. As such, only median lead times for v2 and v1 for various thresholds of Ref_{-10}, MESH, and VIL are provided in Table 6. The most significant difference between the CTC versions was toward smaller median lead times from v2 compared to v1 for the 23 days studied. This trend is not unexpected given that the added v2 data points are a result of including τ_{vis} trends, which occur at a slightly later stage in the storm's development and that the strongest cooling rates are more reliably detected (occur later than the preceding weaker CTC). The slight decrease in lead time does not limit the usefulness of v2 data, as demonstrated at the 2012–3 NOAA HWT (GOES-R Proving Ground 2013), especially given the increased algorithm skill for operationally significant echoes.

4. Summary

The use of remote sensing data with high spatial and high temporal resolution is essential when monitoring the development and growth of deep convective storms. The University of Wisconsin Cloud-Top Cooling Rate algorithm was developed to monitor the vertical growth rate of developing convective clouds by diagnosing regions of cooling IRW BTs between consecutive GOES imager scans. Feedback from various experiments with operational meteorologists indicated the largest deficiency of the v1 algorithm was the inability to diagnose cooling rates in regions of thin cirrus clouds. The v1 algorithm was designed to exclude regions dominated by cirrus clouds because cooling IRW BTs in regions of cumulus cloud growth shielded by upper-level cirrus clouds can be ambiguous in the absence of additional information. To address this deficiency, the CTC algorithm was modified to include τ_{vis} retrievals. The inclusion of τ_{vis} retrievals (v2) increased the

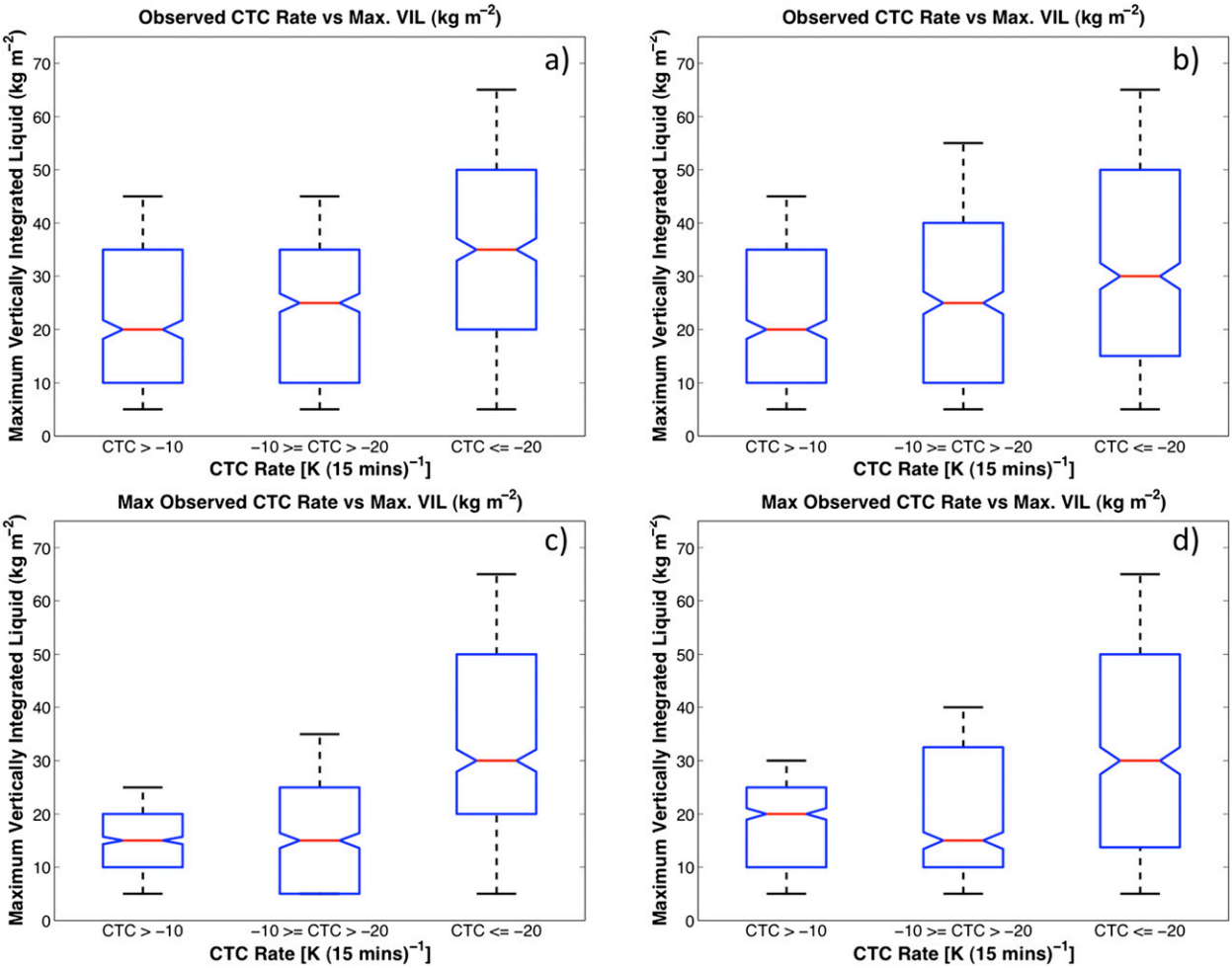

FIG. 6. As in Fig. 4, but for comparison with VIL (kg m^{-2}).

identification of developing storms that were otherwise missed by v1.

A skill score analysis compared the output of v1 and v2 with many NEXRAD fields and thresholds (Ref_{-10}, MESH, and VIL) for 23 convectively active days during spring–early summer 2008 and 2009. It is important to reiterate the skill analysis of v2 applies to the daytime—when visible optical depth retrievals are available. Near the terminator and at night the v1 logic applies and the v1 skill scores and results from H13 best describe the algorithm performance during those conditions. The skill score analysis shows that the inclusion of τ_{vis} into the CTC algorithm acts to increase PODs for all thresholds of all NEXRAD fields analyzed, especially for strong/intense values of those fields [e.g., PODs for 50-, 55-, and 60-dBZ Ref_{-10} for v2 (v1) are 0.44 (0.38), 0.57 (0.48), and 0.71 (0.58), respectively]. The CSI was shown to slightly increase for most thresholds of the NEXRAD fields for v2 relative to v1, with more notable CSI increases for strong CTC and strong/intense Ref_{-10}, MESH, and VIL. The analysis also demonstrated that v2 more often identified the strongest vertical growth rate (cooling rate), whereas v1 sometimes missed the strongest cloud-top cooling rate as a result of specific algorithm configuration (e.g., ice cloud percentage test). The more complete identification of the strongest cloud-top cooling rates with v2 acted to narrow the distributions of maximum CTC and maximum NEXRAD values and shift those distributions to more intense (weak) NEXRAD values for strong (weak) CTC bins relative to v1 (even in regions absent of thin cirrus shields). In practical terms, a forecaster can have increased confidence in the following: 1) developing storms with strong CTC values will more often be associated with future strong/intense NEXRAD observations, while storms with weak CTC values will more often fail to reach strong/intense NEXRAD values; 2) the strongest cloud-top cooling rate of a developing storm will more often be successfully

TABLE 6. Median lead time (min) of maximum CTC hits for v2 and v1 vs for various thresholds of Ref_{-10}, MESH, and VIL (Tables 1, 4, and 5, respectively) for storms during the 23 convective afternoons studied. The lead-time analysis was bounded by a maximum lead time of 60 min; hence, the use of 60+ in these situations to reflect that the actual lead time may have exceeded 60 min.

NEXRAD field		v2	v1
Ref_{-10} (dBZ)	35	13	21
	45	20	26
	50	25	32
	55	31	39
	60	41	49
	65	60+	60+
MESH (in.)	0.25	28	36
	0.50	33	41
	0.75	38	58
	1.00	51	60+
	1.50	60+	60+
VIL (kg m^{-2})	10	23	32
	20	26	36
	30	33	46
	40	44	60+
	50	55	60+

identified; 3) growing cumulus clouds within regions of thin cirrus clouds will more often be detected; and 4) developing storms that will achieve severe radar-estimated hail (1.00+-in. MESH), strong Ref_{-10} (55+ dBZ), and large VIL (30+ kg m^{-2}) will most often exhibit strong CTC with v2 rather than with v1. Additionally, the inclusion of τ_{vis} results in only a small reduction in the lead time of the maximum CTC signal to NEXRAD-observed reflectivity and derived field thresholds. Finally, it is important that the relatively high FARs for intense Ref_{-10}, radar-estimated severe hail (via MESH), and so on are taken in context. The high FAR values are due to 1) the validation domain encompassed regions of expected severe and nonsevere thunderstorms; 2) intense reflectivity, large hail, and so on being rare relative to all thunderstorms; and 3) the satellite-based cloud-tracking validation technique employed being designed to track *into* the mature thunderstorm stage, and not necessarily to radar maturity. Therefore, the database is, to a degree, an underrepresentation of maximum NEXRAD intensity actually achieved. However, given the high POD values of v2 for intense radar signatures [e.g., 0.83 for 1.00+-in. MESH, 0.71 for 60-dBZ Ref_{-10}], when considering the mesoscale and synoptic environmental conditions, in situations favorable for severe weather, a developing storm will likely exhibit strong CTC prior to the onset of intense reflectivity and/or large radar-estimated hail in most cases.

The v2 output has been generated in real time at UW-CIMSS since April 2012 and is available currently via the CIMSS local data manager. More details on how to ingest CTC fields into the Advanced Weather Interactive Processing System (AWIPS) are available online (http://cimss.ssec.wisc.edu/goes_r/proving-ground/awips/ci/index.html), as is "quick look" imagery (http://cimss.ssec.wisc.edu/snaap/convinit/quicklooks/).

Acknowledgments. We are thankful for the opportunity to perform this work under the NOAA GOES Product Assurance Plan (GIMPAP) program, Grant NA10NES4400013. We thank the many NWS forecasters that have used CTC data and provided valuable feedback for improving the algorithm. We are also grateful for the expertise and openness of the GOES-R Cloud Team at NOAA/STAR and UW-CIMSS in incorporating various cloud retrievals into the CTC algorithm.

APPENDIX

List of Key Acronyms and Abbreviations

τ_{vis}	Visible optical depth
BTs	Brightness temperatures
CSI	Critical success index
CTC	Cloud-top cooling
dBZ	Decibels relative to Z
FAR	False alarm ratio
GOES	Geostationary Operational Environmental Satellite
HWT	Hazardous Weather Testbed
IRW	Infrared window
MESH	Maximum expected size of hail
NEXRAD	Next Generation Weather Radar
NOAA	National Oceanic and Atmospheric Administration
NWS	National Weather Service
POD	Probability of detection
Ref_{-10}	Reflectivity at −10°C isotherm
UW-CIMSS	University of Wisconsin Cooperative Institute for Meteorological Satellite Studies
v1	Version 1 of the CTC algorithm
v2	Version 2 of the CTC algorithm
VIL	Vertically integrated liquid
WDSS-II	Warning Decisions Support System—Integrated Information
WFO	Weather Forecast Office
WSR-88D	Weather Surveillance Radar-1988 Doppler

REFERENCES

Adler, R. F., and D. D. Fenn, 1979a: Thunderstorm intensity as determined from satellite data. *J. Appl. Meteor.,* **18,** 502–517.

——, and ——, 1979b: Thunderstorm vertical velocities estimated from satellite data. *J. Atmos. Sci.,* **36,** 1747–1754.

——, M. J. Markus, and D. D. Fenn, 1985: Detection of severe Midwest thunderstorms using geosynchronous satellite data. *Mon. Wea. Rev.,* **113,** 769–781.

Carvalho, L. M. V., and C. Jones, 2001: A satellite method to identify structural properties of mesoscale convective systems based on the maximum spatial correlation tracking technique (MASCOTTE). *J. Appl. Meteor.,* **40,** 1683–1701.

Cintineo, J. L., T. M. Smith, V. Lakshmanan, H. E. Brooks, and K. L. Ortega, 2012: An objective high-resolution hail climatology of the contiguous United States. *Wea. Forecasting,* **27,** 1235–1248.

——, M. J. Pavolonis, J. M. Sieglaff, and A. K. Heidinger, 2013: Evolution of severe and nonsevere convection inferred from GOES-derived cloud properties. *J. Appl. Meteor.,* **52,** 2009–2023.

GOES-R Proving Ground, cited 2013: The GOES-R Proving Ground at the Hazardous Weather Testbed. [Available online at http://goesrhwt.blogspot.com/].

Greene, D. R., and R. A. Clark, 1972: Vertically integrated liquid water—A new analysis tool. *Mon. Wea. Rev.,* **100,** 548–552.

Hartung, D. C., J. M. Sieglaff, L. M. Cronce, and W. F. Feltz, 2013: An intercomparison of UW cloud-top cooling rates with WSR-88D radar data. *Wea. Forecasting,* **28,** 463–480.

Heidinger, A. K., 2011: Algorithm theoretical basis document: ABI cloud mask. NOAA/NESDIS/Center for Satellite Applications and Research Tech. Rep., 93 pp. [Available at http://www.goes-r.gov/products/ATBDs/baseline/Cloud_CldMask_v2.0_no_color.pdf.]

Lakshmanan, V., T. Smith, K. Hondl, G. J. Stumpf, and A. Witt, 2006: A real-time, three-dimensional, rapidly updating, heterogeneous radar merger technique for reflectivity, velocity, and derived products. *Wea. Forecasting,* **21,** 802–823.

——, A. Fritz, T. Smith, K. Hondl, and G. J. Stumpf, 2007: An automated technique to quality control radar reflectivity data. *J. Appl. Meteor. Climatol.,* **46,** 288–305.

Mecikalski, J. R., and K. M. Bedka, 2006: Forecasting convective initiation by monitoring the evolution of moving cumulus in daytime GOES imagery. *Mon. Wea. Rev.,* **134,** 49–78.

——, P. D. Watts, and M. Koenig, 2011: Use of Meteosat Second Generation optimal cloud analysis fields for understanding physical attributes of growing cumulus clouds. *Atmos. Res.,* **102,** 175–190.

Morel, C., and S. Senesi, 2002: A climatology of mesoscale convective systems over Europe using satellite infrared imagery. I: Methodology. *Quart. J. Roy. Meteor. Soc.,* **128,** 1953–1971.

Nakajima, T., and M. D. King, 1990: Determination of optical thickness and effective particle radius of cloud from reflected solar radiation measurements. Part I: Theory. *J. Atmos. Sci.,* **47,** 1878–1893.

NEXRAD Joint System Program Office, 1985: Next generation weather radar (NEXRAD) algorithm report. NEXRAD Joint System Program Office Tech. Rep., 926 pp. [Available online at https://archive.org/stream/nextgenerationwe00nexr#page/n0/mode/1up.]

Ortega, K. L., T. M. Smith, and G. J. Stumpf, 2006: Verification of multi-sensor, multi-radar hail diagnosis techniques. Preprints, *Symp. on the Challenges of Severe Convective Storms,* Atlanta, GA, Amer. Meteor. Soc., P1.1. [Available online at https://ams.confex.com/ams/pdfpapers/104885.pdf.]

Pavolonis, M. J., 2010: GOES-R Advanced Baseline Imager (ABI) algorithm theoretical basis document for cloud type and cloud phase. NOAA/NESDIS/Center for Satellite Applications and Research Tech. Rep., 96 pp. [Available online at http://www.goes-r.gov/products/ATBDs/baseline/Cloud_CldType_v2.0_no_color.pdf.]

Platnick, S., M. D. King, S. A. Ackerman, W. P. Menzel, B. A. Baum, J. C. Riedi, and R. A. Frey, 2003: The MODIS cloud products: Algorithms and examples from Terra. *IEEE Trans. Geosci. Remote Sens.,* **41,** 459–473.

Roberts, R. D., and S. Rutledge, 2003: Nowcasting storm initiation and growth using *GOES-8* and WSR-88D data. *Wea. Forecasting,* **18,** 562–584.

Sieglaff, J. M., L. M. Cronce, W. F. Feltz, K. M. Bedka, M. J. Pavolonis, and A. K. Heidinger, 2011: Nowcasting convective storm initiation using satellite-based box-averaged cloud-top cooling and cloud-type trends. *J. Appl. Meteor. Climatol.,* **50,** 110–126.

——, D. C. Hartung, W. F. Feltz, L. M. Cronce, and V. Lakshmanan, 2013: Development and application of a satellite-based convective cloud object-tracking methodology: A multipurpose data fusion tool. *J. Atmos. Oceanic Technol.,* **30,** 510–525.

Stumpf, G. J., T. M. Smith, and J. Hocker, 2004: New hail diagnostic parameters derived by integrating multiple radars and multiple sensors. Preprints, *22nd Conf. on Severe Local Storms,* Amer. Meteor. Soc., Hyannis, MA, P7.8. [Available online at https://ams.confex.com/ams/pdfpapers/81451.pdf.]

UW-CIMSS, cited 2013: Zoomerang poll results. University of Wisconsin Cooperative Institute for Meteorological Satellite Studies. [Available online at http://cimss.ssec.wisc.edu/goes_r/proving-ground/SPC/UWCI_Feedback.html.]

Vila, D. A., L. A. T. Machado, H. Laurent, and I. Velasco, 2008: Forecasting and Tracking the Evolution of Cloud Clusters (ForTraCC) using satellite infrared imagery: Methodology and validation. *Wea. Forecasting,* **23,** 233–245.

Walther, A., and A. Heidinger, 2012: Implementation of the Daytime Cloud Optical and Microphysical Properties Algorithm (DCOMP) in PATMOS-X. *J. Appl. Meteor. Climatol.,* **51,** 1371–1390.

Witt, A., M. D. Eilts, G. J. Stumpf, J. T. Johnson, E. D. W. Mitchell, and K. W. Thomas, 1998a: An enhanced hail detection algorithm for the WSR-88D. *Wea. Forecasting,* **13,** 286–303.

——, ——, ——, E. D. Mitchell, J. T. Johnson, and K. W. Thomas, 1998b: Evaluating the performance of WSR-88D severe storm detection algorithms. *Wea. Forecasting,* **13,** 513–518.

Zinner, T., H. Mannstein, and A. Tafferner, 2008: Cb-TRAM: Tracking and monitoring severe convection from onset over rapid development to mature phase using multi-channel *Meteosat-8* SEVIRI data. *Meteor. Atmos. Phys.,* **101,** 191–210.